The Modulation of Equatorial Turbulence by Tropical Instability Waves in a Regional Ocean Model

Journal of Physical Oceanography, 2015, 45 (4), 1155-1173

R. Holmes and L. Thomas

SPECIAL Ocean Turbulence COLLECTION

The Modulation of Equatorial Turbulence by Tropical Instability Waves in a Regional Ocean Model

R. M. HOLMES AND L. N. THOMAS

Environmental Earth System Science, Stanford University, Stanford, California

(Manuscript received 9 October 2014, in final form 8 January 2015)

ABSTRACT

Small-scale turbulent mixing in the upper Equatorial Undercurrent (EUC) of the eastern Pacific cold tongue is a critical component of the SST budget that drives variations in SST on a range of time scales. Recent observations have shown that turbulent mixing within the EUC is modulated by tropical instability waves (TIWs). A regional ocean model is used to investigate the mechanisms through which large-scale TIW circulation modulates the small-scale shear, stratification, and shear-driven turbulence in the EUC. Eulerian analyses of time series taken from both the model and the Tropical Atmosphere Ocean (TAO) array suggest that increases in the zonal shear of the EUC drive increased mixing on the leading edge of the TIW warm phase. A Lagrangian vorticity analysis attributes this increased zonal shear to horizontal vortex stretching driven by the strain in the TIW horizontal velocity field acting on the existing EUC shear. To investigate the impact of horizontal vortex stretching on the turbulent heat flux averaged over a TIW period the effects of periodic TIW strain are included as forcing in a simple 1D mixing model of the EUC. Model runs with TIW forcing show turbulent heat fluxes up to 30% larger than runs without TIW forcing, with the magnitude of the increase being sensitive to the vertical mixing scheme used in the model. These results emphasize the importance of coupling between the large-scale circulation and small-scale turbulence in the equatorial regions, with implications for the SST budget of the equatorial Pacific.

1. Introduction

Small-scale turbulent mixing of heat in the tropical Pacific is an important component of the sea surface temperature (SST) budget and contributes to changes in SST over a range of time scales. Variations in diapycnal turbulent transport play a role in the seasonal cycle of SST (Moum et al. 2013) and the diurnal cycle in SST (Bernie et al. 2005; Danabasoglu et al. 2006). Modulations in turbulence at time scales of weeks to months associated with intraseasonal Kelvin waves (Lien et al. 1995; McPhaden 2002), the Madden–Julian oscillation (Chi et al. 2014), and tropical instability waves (TIWs) (Menkes et al. 2006; Moum et al. 2009; Inoue et al. 2012) may have an important impact on the mean state of the Pacific Ocean and thus on global climate.

Generated in the eastern tropical Pacific and Atlantic Oceans, TIWs propagate westward with wavelengths of 700–1600 km and periods of 15–40 days (Qiao and Weisberg 1995; Kennan and Flament 2000; Willett et al. 2006; Lyman et al. 2007). TIWs are generated through barotropic and baroclinic instability of the mean equatorial current system (Philander 1976; Cox 1980; Masina et al. 1999; Lyman et al. 2005) and vary seasonally and interannually, obtaining peak amplitudes in boreal fall and winter and in La Niña conditions (Contreras 2002; An 2008). Near the equator, TIW meridional advection of the equatorial fronts results in variations of several degrees Celsius in SST, organized into alternating warm and cold phases. TIWs and their associated vortices [tropical instability vortices (TIVs)] drive lateral heat fluxes that warm the cold tongue by $\sim$1°C month^{-1} (Menkes et al. 2006; Jochum et al. 2007; Graham 2014), potentially contributing to the asymmetry of the ENSO cycle (An 2008; Imada and Kimoto 2012). Jochum and Murtugudde (2006) suggested that TIWs warm the cold tongue not through typical eddy mixing, but instead

Corresponding author address: R. M. Holmes, Environmental Earth System Science, 473 Via Ortega, Room 140, Stanford University, Stanford, CA 94305.
E-mail: rmholmes@stanford.edu

DOI: 10.1175/JPO-D-14-0209.1

through modifications of the air–sea fluxes and vertical entrainment. The modifications of air–sea fluxes by TIWs have received considerable attention (Thum et al. 2002; Seo et al. 2007; Small et al. 2009), while the modifications of vertical entrainment by TIWs have been observed only recently.

These observations have shown that TIWs modulate vertical mixing in the upper Equatorial Undercurrent (EUC) (Lien et al. 2008; Moum et al. 2009; Inoue et al. 2012). Here, the gradient Richardson number (Ri) of the flow is preconditioned to drop below the critical value for shear instability of 1/4, where

$$\mathrm{Ri} = N^2 \Big/ \left[\left(\frac{\partial u}{\partial z}\right)^2 + \left(\frac{\partial v}{\partial z}\right)^2\right], \qquad (1)$$

$N^2 = \partial b/\partial z$ is the buoyancy frequency squared, $b = -g\rho/\rho_0$ is the buoyancy, g is the acceleration due to gravity, ρ is the potential density, ρ_0 is a reference density, and u, v are the zonal and meridional velocities, respectively. A telltale signature that shear instabilities have been active is for a flow to be in a state of marginal stability, where the Richardson number is close to 1/4 and the reduced shear squared,

$$\mathrm{Sh}^2_{\mathrm{red}} \equiv \left(\frac{\partial u}{\partial z}\right)^2 + \left(\frac{\partial v}{\partial z}\right)^2 - 4N^2, \qquad (2)$$

is near zero. Indeed, observations show that for three-quarters of the year, the upper EUC is in this state (Smyth and Moum 2013). Using a Lagrangian float, Lien et al. (2008) observed that the vertical entrainment flux at the base of the mixed layer varied with the TIW phase along the equator, with the highest values occurring leading into the TIW warm phase. They attributed this increase in entrainment flux to an increase in the $\mathrm{Sh}^2_{\mathrm{red}}$ and pointed out that it could not be explained by variations in wind-driven mixing. More recently, Inoue et al. (2012) observed modifications of deep-cycle turbulence (a layer of strong turbulence below the mixed layer that shows a distinct diurnal cycle), mixed layer depth, and the turbulent heat flux with TIW phase using a 2-week time series of microstructure profiles at 0°, −140°E. Their measurements show that the highest values of $\mathrm{Sh}^2_{\mathrm{red}}$, dissipation, and turbulent heat flux occur at the leading edge of the TIW warm phase when the meridional velocity switches from northward to southward, consistent with the observations of Lien et al. (2008).

The mechanism through which TIWs modulate small-scale turbulent mixing is not known. Moum et al. (2009) hypothesized that the extra meridional shear added by TIWs can push the marginally stable reduced shear squared above the EUC core over the threshold for shear instability producing stronger turbulence. However, the meridional shear associated with TIWs is significantly weaker than the zonal shear in this region [see Fig. 4 of Inoue et al. (2012)]. TIWs also influence both zonal velocities and the density field near the equator (Lyman et al. 2007; Jochum et al. 2007; Inoue et al. 2012), suggesting that other processes may be at play. It is also unclear if TIW-induced variations in mixing lead to a net cooling or warming of equatorial SSTs. Moum et al. (2009) observed turbulent mixing associated with TIWs that drove surface cooling of 1°–2°C month^{-1}. In contrast, the modeling study of Menkes et al. (2006) found that variations in the vertical turbulent entrainment flux on TIW time scales had a rectified warming influence of 0.37°C month^{-1}. In this article, we identify the mechanism responsible for the modulation of mixing by TIWs in a regional ocean model of the equatorial Pacific with a highly resolved TIW field. These simulations are combined with a one-dimensional (1D) vertical mixing model to quantify the net turbulent heat fluxes associated with TIWs and assess their sensitivity to the vertical mixing parameterization scheme.

The article is organized as follows: Section 2 describes the ocean model and evaluates its performance in the upper EUC in comparison to observations from the Tropical Atmosphere Ocean (TAO) mooring array (McPhaden et al. 1998). Section 3 examines the factors influencing mixing on TIW time scales in the upper EUC, using both the model and TAO data. Section 4 examines the dynamics behind the modulation of mixing by TIWs using a Lagrangian analysis. Section 5 examines the total influence of TIWs on the turbulent heat flux using a simple 1D mixing model of the EUC, and section 6 discusses and summarizes the results.

2. Model and general flow description

This section describes the ocean model setup (section 2a) and its main features, evaluates its performance in comparison to observations (section 2b), and discusses a feature of the observations not well represented in the model, that of marginal stability (section 2c).

a. Ocean model setup

In this article, we analyze results from a set of 3D nested simulations of the equatorial Pacific performed with the Regional Ocean Modeling System (ROMS) (Shchepetkin and McWilliams 2005). The outer nest is a Pacific basinwide simulation over the region 30°S to 30°N, −240° to −70°E with 0.25° horizontal resolution, 50 vertical levels, and a time step of 10 min. It was spun up for 5 yr, initialized from a previous 10-yr spinup run (Holmes et al. 2014). Daily climatological surface forcing, initial conditions, and boundary conditions were taken from the Common Ocean Reference Experiment Normal Year Forcing field (Large and Yeager 2004). In addition, a diurnal cycle in shortwave radiation was imposed, as we found this was necessary to produce the appropriate shear and stratification in and near the mixed layer (not shown), consistent with the studies of Kawai and Wada (2007) and Bernie et al. (2007). At the meridional boundaries, temperature and salinity were nudged to climatological values, while zonal and meridional velocities were nudged to zero. Monthly climatological nudging was used in the western Pacific warm pool in order to maintain the tropical pycnocline. The K-profile parameterization (KPP) vertical mixing scheme was used to parameterize subgrid-scale vertical mixing processes (Large et al. 1994). Its role is discussed further in sections 2c and 5.

To perform Lagrangian particle advection and analyze Lagrangian shear and stratification budgets (section 4), a high-resolution simulation was nested offline inside the last year of the basinwide simulation over the region 5°S to 10°N, $-155°$ to $-120°$E. This nest has a horizontal resolution ($1/20°$, ~6 km) below the 10 km reported by Marchesiello et al. (2011), as required for numerical convergence as measured by an invariance of the kinetic energy spectrum with resolution. In the high-resolution simulation, a combination of nudging and radiation boundary conditions was used, with the exception of a clamped condition on the eastern boundary for tracers. These boundary conditions were taken from the outer nest at daily resolution. Horizontal diffusion of momentum was achieved with a biharmonic viscosity with the coefficients $1 \times 10^{10}\,\mathrm{m^4\,s^{-1}}$ (high resolution) and $1 \times 10^{11}\,\mathrm{m^4\,s^{-1}}$ (basinwide), and the harmonic horizontal diffusion of salinity and temperature was included with a coefficient of $100\,\mathrm{m^2\,s^{-1}}$. ROMS has been successfully used for process studies of TIWs under similar configurations (Marchesiello et al. 2011; Holmes et al. 2014). In the next subsection, we discuss the general features of the model near the equator and evaluate the model performance by comparison to observations from the TAO array.

b. General flow description and evaluation of model performance

The model produces vigorous TIWs with meridional velocities reaching $0.5\,\mathrm{m\,s^{-1}}$ on the equator (Fig. 1b) that advect the north equatorial front across the equator, inducing SST variations of the order of 2°C (Figs. 1a, 2), consistent with the findings of Qiao and Weisberg (1995) and Inoue et al. (2012). North of the equator, TIVs centered around 4°N are characterized by an anticyclonic circulation with vorticity close to $-f$ (f is the Coriolis parameter) that induces variations in zonal velocity and stratification (Holmes et al. 2014; Fig. 2). These features and the spatial structure of the TIWs and TIVs are consistent with the observations of Qiao and Weisberg (1995) and Kennan and Flament (2000).

In this article, we focus on the upper EUC shear layer between the EUC core and the mixed layer, where the shear, stratification, and $\mathrm{Sh}^2_{\mathrm{red}}$ are largest (Figs. 1c–e,g, 2a–c). This layer contains the turbulent deep cycle and upper-core layers observed by Inoue et al. (2012). These are manifest in the model as an enhancement of the daily averaged vertical diffusivity, which reaches values $>10^{-3}\,\mathrm{m^2\,s^{-1}}$ at these depths (Fig. 2d). The model contains variations in a number of properties, including the $\mathrm{Sh}^2_{\mathrm{red}}$, with TIW phase. These modulations are discussed in section 3.

Profiles of model vertical shear and stratification averaged over the TIW season (September–December) of the last year of the basinwide simulation compare favorably with data taken from the TAO array mooring at 0°, $-140°$E (Fig. 3). The TAO data are averaged over the neutral ENSO years 1996, 2001, 2003, and 2005. The zonal shear in the model compares well with the TAO data in the upper EUC shear layer (cf. red dashed line with black line in Fig. 3a), but the shear below the EUC core is too weak. The average EUC core depth is 10 m too deep in the model (134 m in ROMS vs 122.5 m in the TAO observations). The stratification is stronger in the surface layer, and the pycnocline is slightly weaker in the model (cf. red dashed line with black line in Fig. 3b). However, the stratification due to salinity is not included in the observations, and the profile of stratification due to salinity from the model (green dashed line in Fig. 3b) suggests that the comparison may be improved if salinity data from the TAO mooring were available. The model $\mathrm{Sh}^2_{\mathrm{red}}$ compares well with the observations throughout the upper 150 m where data are available. Above 80 m, the mean $\mathrm{Sh}^2_{\mathrm{red}}$ is close to zero in both the observations and the model, in agreement with the observations of Smyth and Moum (2013). However, the daily averaged $\mathrm{Sh}^2_{\mathrm{red}}$ does reach positive values on some occasions, as discussed in the next section.

c. Marginal stability

In the model, the daily averaged $\mathrm{Sh}^2_{\mathrm{red}}$ occasionally reaches positive values well above the criteria for K–H instability (Figs. 1g, 2c). Smyth and Moum (2013) showed that 6-hourly averaged profiles of the Richardson number in the upper EUC remain in a state of marginal stability, a characteristic not reproduced by the model. In these regions the KPP vertical diffusivity (Fig. 2d) approaches its maximum interior value of $K_0 = 2 \times 10^{-3}\,\mathrm{m^2\,s^{-1}}$ (see section 5). This suggests that the mixing scheme is not able to provide enough mixing at

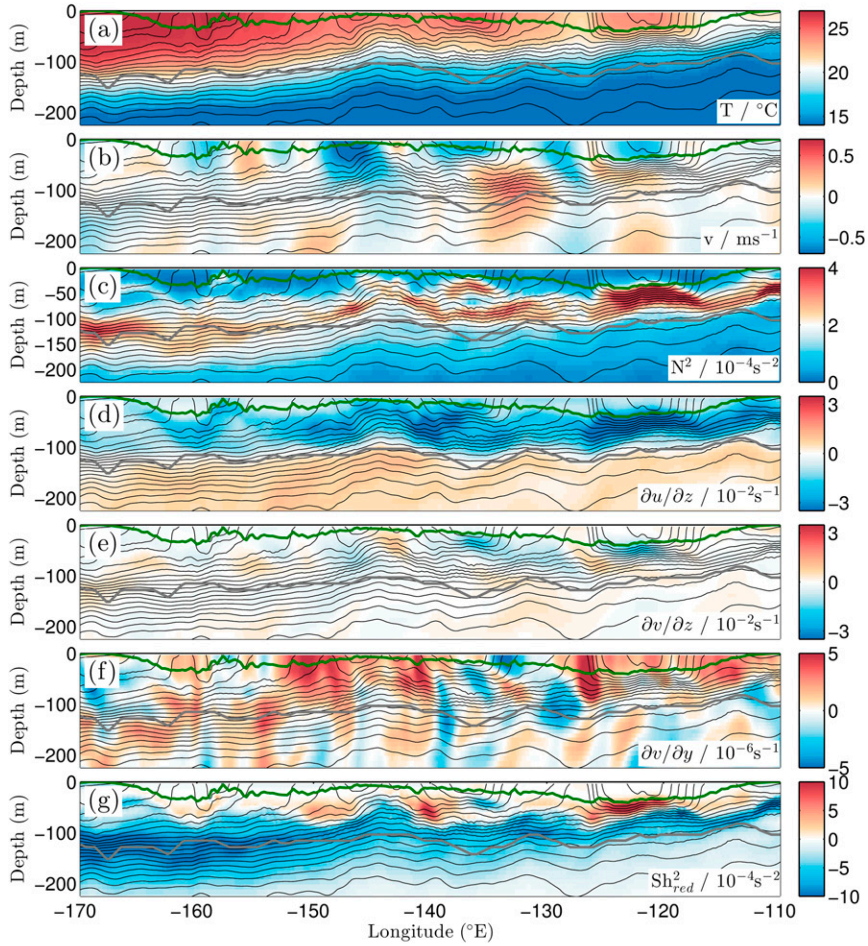

FIG. 1. Daily averaged (a) temperature, (b) meridional velocity, (c) stratification, (d) zonal shear, (e) meridional shear, (f) meridional diffluence, and (g) reduced shear squared along the equator on yearday 262.5 of the basinwide ROMS simulation. The dark green lines indicate the depth of the KPP mixed layer, the gray lines indicate the depth of the EUC core, and the black contours are isopycnals at 0.2 kg m^{-3} spacing. High $\mathrm{Sh}^2_{\mathrm{red}}$ generally occurs at the leading edge of a TIW warm phase and is accompanied by high zonal shear and preceded by meridional diffluence.

high $\mathrm{Sh}^2_{\mathrm{red}}$ in order to restrict the $\mathrm{Sh}^2_{\mathrm{red}}$ to negative or near-zero daily averaged values.

To evaluate the influence of this issue on our results, we constructed an algorithm to enforce marginal stability offline for all regions in the simulations where $\mathrm{Sh}^2_{\mathrm{red}} > 0$. The algorithm is similar to the Price et al. (1986) mixing scheme and iteratively applies vertical fluxes of temperature, salinity, and momentum in a Prandtl number one ratio until regions of $\mathrm{Sh}^2_{\mathrm{red}} > 0$ are removed, subject to the constraints of conservation of heat, salt, and momentum (see the appendix for a description of the algorithm). The resulting profiles have regions of marginal stability (Fig. 4; between 100 m and the surface) bordered by thin regions with strong momentum and buoyancy gradients (Fig. 4; near 100 m), in agreement with theories of eddy-driven mixing (Holzer and Siggia 1994). This algorithm will be used in sections 3 and 4 to evaluate the impact of not enforcing marginal stability on our results. The KPP interior mixing parameterization for shear instability and its relation to marginal stability are examined in more detail in section 5.

3. Eulerian analysis of TIW modulation

This section examines the variations in shear, stratification, and mixing on TIW time and length scales. Temperature, velocity, vertical shear, and stratification all vary around their mean state along the equator as a function of TIW phase (Figs. 1, 2). The highest $\mathrm{Sh}^2_{\mathrm{red}}$, where the most mixing is expected, occurs on the leading

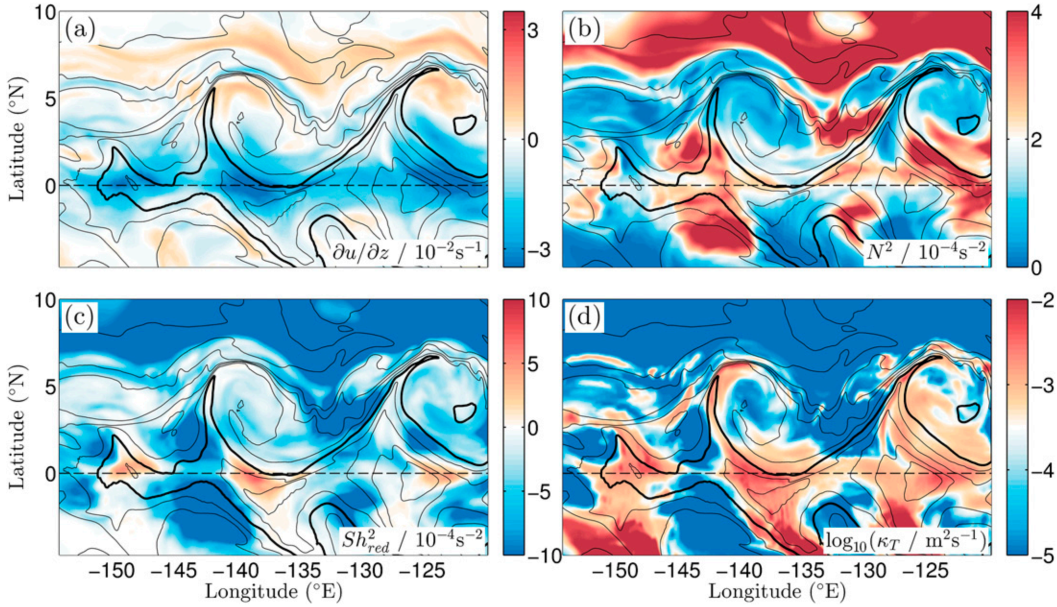

FIG. 2. Daily averaged (a) zonal shear, (b) stratification, (c) reduced shear squared, and (d) vertical diffusivity at 72-m depth on yearday 262.5 of the high-resolution ROMS simulation. Also shown are contours of SST at 0.75°C intervals, with the 25° isotherm highlighted in thickness. The dashed line indicates the equator. In (c), three patches of high $\mathrm{Sh}^2_{\mathrm{red}}$ are visible at the leading edge of TIW warm phases.

edge of TIW-induced warm perturbations (Fig. 2c), highlighted by near-surface bowl-shaped isopycnals (Figs. 1a,g; near −159°, −149°, −141°, and −125°E). This is in agreement with the observations of Lien et al. (2008). This phase of the TIW generally corresponds to a change in meridional velocity from northward to southward (Fig. 1b), in agreement with the observations of Inoue et al. (2012). Each component of the $\mathrm{Sh}^2_{\mathrm{red}}$, the stratification, zonal shear, and meridional shear (Figs. 1c–e) varies at TIW length scales along the equator. While the variations in meridional shear (Fig. 1e) are the clearest, they are weaker in magnitude than the variations in zonal shear and stratification and are not clearly correlated with the $\mathrm{Sh}^2_{\mathrm{red}}$ (cf. Figs. 1e and 1g near patches of high $\mathrm{Sh}^2_{\mathrm{red}}$). While the stratification shows large variations relative to its mean, it appears to be stronger in patches of high $\mathrm{Sh}^2_{\mathrm{red}}$ (cf. Figs. 1c and 1g). The zonal shear also shows large variations relative to its mean, with strongly negative zonal shear patches closely correlated with high $\mathrm{Sh}^2_{\mathrm{red}}$ patches (cf. Fig. 1d with Fig. 1g and Fig. 2a with Fig. 2c). This suggests that increases in zonal shear are responsible for the patches of high $\mathrm{Sh}^2_{\mathrm{red}}$.

To quantitatively analyze temporal variations in the shears, stratification, and mixing due to TIWs, we calculated their root-mean-square (RMS) variation over the TIW frequency band by taking the square root of the total power between periods of 5 and 50 days from the power spectrum of the time series at each depth at 0°, −140°E (Figs. 3c,e,f). Average RMS values were also obtained from the TAO observations by calculating individual spectra for September–December of each year. The shape of the profiles and the comparative results were found to be insensitive to the frequency window used. The vertical motion of the EUC core did not influence the results discussed below, as tested by calculating the RMS values in EUC core relative depth coordinates (not shown).

There are strong temporal variations in $\mathrm{Sh}^2_{\mathrm{red}}$ at TIW frequencies (Fig. 3e), with the RMS value approaching the magnitude of the mean $\mathrm{Sh}^2_{\mathrm{red}}$ (cf. Figs. 3e and 3d). As for the variations with longitude (Fig. 1), the temporal variations in $\mathrm{Sh}^2_{\mathrm{red}}$ at 0°, −140°E are because of variations in zonal shear squared [$\mathrm{RMS}_{(\partial u/\partial z)^2}$ in Fig. 3c] and stratification (Fig. 3f). The variations in meridional shear squared [$\mathrm{RMS}_{(\partial v/\partial z)^2}$ in Fig. 3c] at TIW frequencies are much weaker than the other components in both model and observations. This suggests that TIW meridional shear is not directly responsible for the modulation of vertical mixing, contrary to the hypothesis of Moum et al. (2009). Jing et al. (2014) also noted that temporal variations in the amplitude of 2-h–8-day oscillations in the upper EUC, potentially linked to higher-frequency motions and turbulence, were more correlated with variations in the EUC zonal shear than with the meridional shear of TIWs.

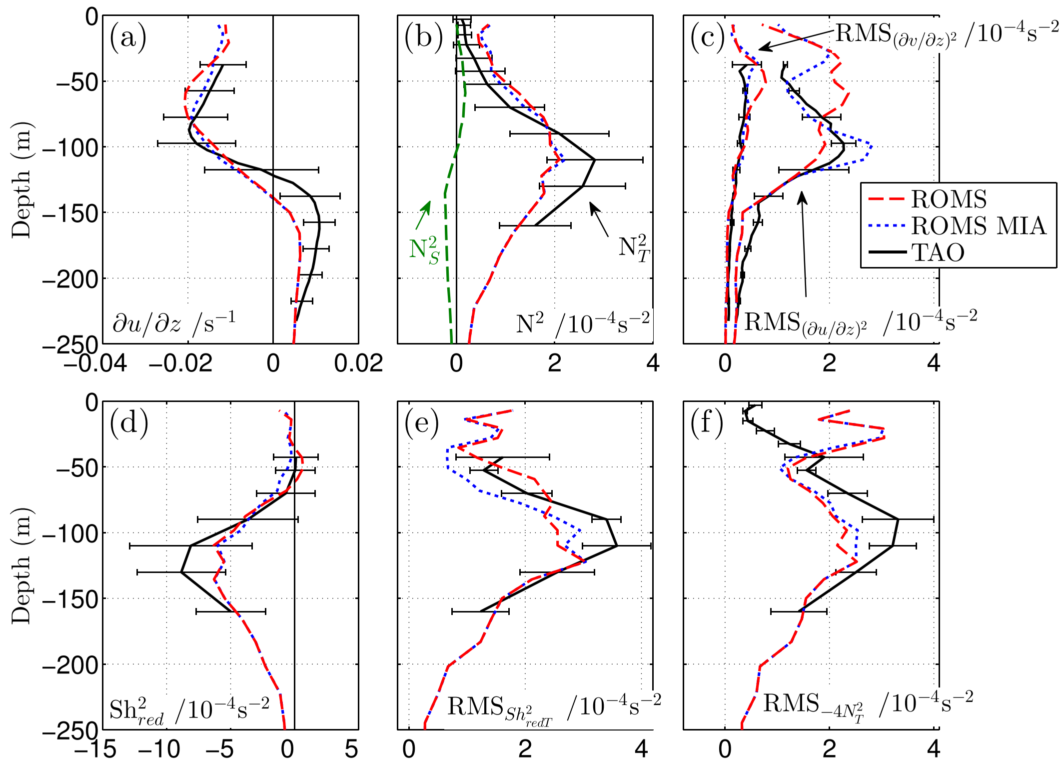

FIG. 3. Comparison of mean profiles at 0°, −140°E from the TAO array mooring (black lines) with the basinwide ROMS simulation without and with adjustment to marginal stability (red dashed and blue dotted lines, respectively). The profiles are averaged over the September–December period. The TAO data are averaged over the neutral ENSO years 1996, 2001, 2003, and 2005. (a) Mean zonal velocity shear and (b) mean stratification, where the green dotted N_S^2 line indicates the buoyancy gradient due only to salinity in ROMS. The TAO data N_T^2 are calculated only with temperature. (d) Mean reduced shear squared. RMS temporal variations in the (c) zonal and meridional shear squared, (e) reduced shear squared using only temperature stratification, and (f) temperature stratification. The RMS values are obtained by taking the square root of the total power between the frequencies 1/50 and 1/5 day^{-1} calculated from the power spectrum of the respective variables in the months September–December. The error bars represent the $\pm 2\sigma$ standard error spread over the four neutral ENSO years included in the TAO calculation.

The model and observed RMS values agree well below the surface layer (cf. red dashed lines and black lines in Figs. 3c,e,f). The temporal variation in stratification (Fig. 3f) is weaker in the model than the observations, which may be a result of the weaker thermocline in the model (Fig. 3b). The largest discrepancy between model and observations is in the temporal variations in zonal shear squared in the upper EUC between 120 and 40 m (cf. red dashed and black lines in Fig. 3c). The vertical structure is different, with the model zonal shear varying too much in the upper half of this region and too little in the lower half. These differences were traced to the failure of the KPP interior mixing scheme to enforce marginal stability.

RMS profiles calculated using the marginal stability adjustment algorithm (see the appendix) are more similar to the observations (blue dotted lines in Fig. 3). The mean quantities show only small improvements, with a reduction in the mean zonal shear, stratification, and $\mathrm{Sh}^2_{\mathrm{red}}$ between 75 and 40 m as a result of the additional mixing (cf. blue dotted to red dashed lines in Figs. 3a,b,d). However, the RMS variation in zonal shear squared shows large changes, with a reduction between 85 and 40 m and an increase around 100 m (cf. blue dotted line and red dashed line in Fig. 3c), consistent with the mixing and expulsion of gradients from regions with $\mathrm{Sh}^2_{\mathrm{red}} > 0$. Corresponding to the changes in zonal shear squared variations, there are changes to variations in $\mathrm{Sh}^2_{\mathrm{red}}$ (Fig. 3e), with only minimal changes to variations in stratification (Fig. 3f).

Temporal variations in zonal shear squared and stratification are similar in magnitude (cf. Figs. 3c and 3f), suggesting that they are equally important in driving modulations in the $\mathrm{Sh}^2_{\mathrm{red}}$. However, the patches of high $\mathrm{Sh}^2_{\mathrm{red}}$, and thus high mixing, are generally associated with high shear magnitudes and relatively high stratification (e.g., compare Figs. 1c,d,g and Figs. 2a,b,c near patches of high $\mathrm{Sh}^2_{\mathrm{red}}$), as opposed to anomalies of low

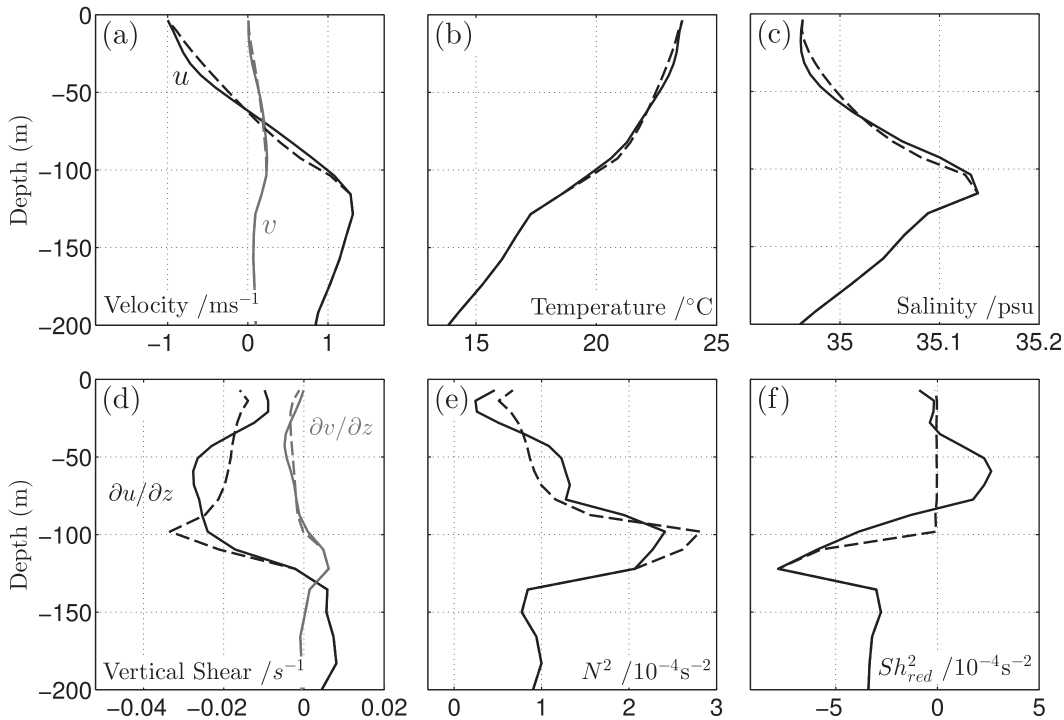

FIG. 4. Vertical profiles of (a) velocity, (b) temperature, (c) salinity, (d) vertical shear, (e) stratification, and (f) reduced shear squared at 0°, −140°E on yearday 268.5 from the model. The solid lines show the original profiles, and the dashed lines show the profiles after adjustment to marginal stability ($\mathrm{Sh}^2_{\mathrm{red}} = 0$) for unstable regions ($\mathrm{Sh}^2_{\mathrm{red}} > 0$) using the algorithm described in the appendix. Note the reduction in shear and stratification in the unstable region between 40- and 80-m depth, and the consequent accumulation of shear and stratification on the edges of this region.

stratification and low shear. This suggests that the patches of high mixing are driven by increases in shear, as opposed to decreases in stratification. This hypothesis is supported by the Lagrangian diagnostic analyses performed in the next section.

4. Lagrangian analysis of high mixing patches

In this section, we examine the dynamical processes responsible for the increase in $\mathrm{Sh}^2_{\mathrm{red}}$ on the leading edge of the TIW warm phase. We analyze a set of Lagrangian particles that entered a patch of high $\mathrm{Sh}^2_{\mathrm{red}}$ located at −139°E on yearday 262.5 (Fig. 5). The particles were chosen by first advecting particles seeded within the patch of high $\mathrm{Sh}^2_{\mathrm{red}}$ backward in time to identify the source regions of the high $\mathrm{Sh}^2_{\mathrm{red}}$ and then evenly seeding particles across these regions for a forward in time Lagrangian calculation. A subset of these particles was then chosen that had $\mathrm{Sh}^2_{\mathrm{red}} > 2 \times 10^{-4}\,\mathrm{s}^{-2}$ and that were located in the upper EUC shear layer between depths of 120 and 30 m on yearday 262.5. The particles satisfying these conditions were sourced from two different water masses. Of all the particles, 88% entered the region of high $\mathrm{Sh}^2_{\mathrm{red}}$ from the west through the EUC (black EUC particles in Fig. 5). The other 12% of particles entered the region of high $\mathrm{Sh}^2_{\mathrm{red}}$ from the east from a nearby TIV (white TIV particles in Fig. 5). The TIV particles entered higher in the water column, reflecting the negative vertical shear in zonal velocity in the upper EUC, the westward flow of the southern portion of the TIV, and the warmth and lighter density of the TIV water mass in comparison to the equatorial water.

The $\mathrm{Sh}^2_{\mathrm{red}}$ following this set of particles (green line in Fig. 6a) increases rapidly in time to values above zero, and thus the presence of high $\mathrm{Sh}^2_{\mathrm{red}}$ in the high mixing patch is not a result of advection. This increase in $\mathrm{Sh}^2_{\mathrm{red}}$ is because of a rapid increase in zonal shear squared (black line in Fig. 6a), as the stratification stays relatively constant (blue line in Fig. 6a) and the meridional shear squared is small (red line in Fig. 6a). This is consistent with the Eulerian analysis in the previous section.

To determine the cause of the increase in zonal shear, we perform a Lagrangian budget of zonal shear along the particle tracks. The zonal shear satisfies

$$\frac{D}{Dt}\left(\frac{\partial u}{\partial z}\right) = \frac{\partial u}{\partial z}\frac{\partial v}{\partial y} + \left(f - \frac{\partial u}{\partial y}\right)\frac{\partial v}{\partial z} - \frac{\partial b}{\partial x} + \frac{\partial F_x}{\partial z}, \quad (3)$$

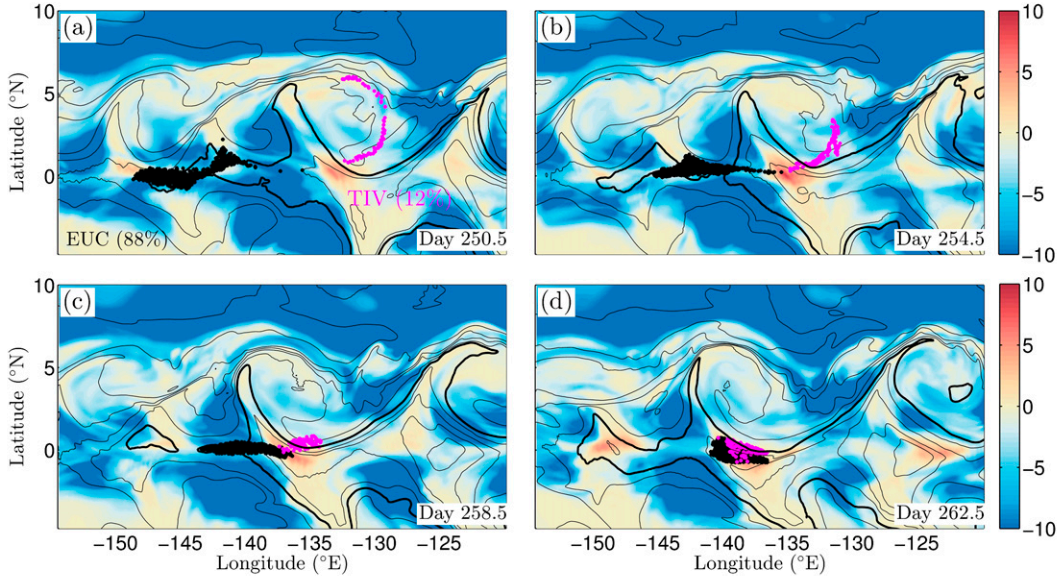

FIG. 5. Daily averaged Sh^2_{red} ($10^{-4}\,s^{-2}$) in the upper EUC at 72-m depth at four different times separated by 4 days from the high-resolution simulation. The contours are SST at 0.75°C intervals, with the 25°C isotherm thicker. Shown are the positions of Lagrangian particles that enter the patch of high Sh^2_{red} at 0°, −140°E on (d) day 262.5. These Lagrangian particles are identified either as EUC particles (893 particles composing 88% of the total), if they enter the region from the west through the EUC, or TIV particles (123 particles composing 12% of the total), if they enter the region from the east.

which is equivalent to the equation for the north–south component of the vorticity for the primitive equations, where F_x is the frictional force in the zonal direction. Integrating along a particle path from a time t_0 to t gives

$$\frac{\partial u}{\partial z}(t)-\frac{\partial u}{\partial z}(t_0)=\underbrace{\int_{t_0}^{t}\frac{\partial u}{\partial z}\frac{\partial v}{\partial y}\,d\tau}_{\text{STR}}+\underbrace{\int_{t_0}^{t}\left(f-\frac{\partial u}{\partial y}\right)\frac{\partial v}{\partial z}\,d\tau}_{\text{TILT}}\underbrace{-\int_{t_0}^{t}\frac{\partial b}{\partial x}\,d\tau}_{\text{BTOR}}+\underbrace{\int_{t_0}^{t}\frac{\partial F_x}{\partial z}\,d\tau}_{\text{FRIC}}\,. \tag{4}$$

Thus, a change in zonal shear following a particle can be attributed to horizontal vortex stretching (STR), vortex tilting (TILT), the baroclinic torque (BTOR), or frictional torques (FRIC). We analyze these terms along the particle tracks shown in Fig. 5, where we choose t_0 as day 253.5. The terms are calculated by taking the vertical derivative of the zonal momentum equation diagnostics output of ROMS. The numerical accuracy of these calculations were checked by comparing each quantity against the same quantities calculated directly using finite-difference derivatives of the velocity and buoyancy, which gave closely consistent results (not shown).

The dominant process driving an increase in the magnitude of the zonal shear as the particles enter the high mixing patch is horizontal vortex stretching (STR in Fig. 6b). Vortex tilting and the baroclinic torque are negligible (TILT and BTOR in Fig. 6b). The increase in Sh^2_{red} drives an increase in vertical mixing that acts to decrease the magnitude of the shear, as shown by the positive frictional torque (FRIC in Fig. 6b). However, the KPP mixing scheme does not provide enough mixing to enforce marginal stability against the horizontal vortex stretching. Equivalent Lagrangian curves calculated by taking finite-difference derivatives of the model variables adjusted for marginal stability (using the algorithm described in the appendix) show that the additional mixing provided by this algorithm drives a decrease in stratification and limits the increase in zonal shear (dashed curves in Figs. 6a,b). The strength of horizontal vortex stretching also decreases because it depends on the shear itself (dashed magenta curve in Fig. 6b). However, horizontal vortex stretching remains the driver behind the increase in mixing, which now manifests itself as a low stratification anomaly. Further Lagrangian analyses of other patches of high mixing confirm the ubiquity of this mechanism (not shown).

Horizontal vortex stretching here relies on meridional diffluence $\partial v/\partial y > 0$ [see STR in Eq. (4)] away from the

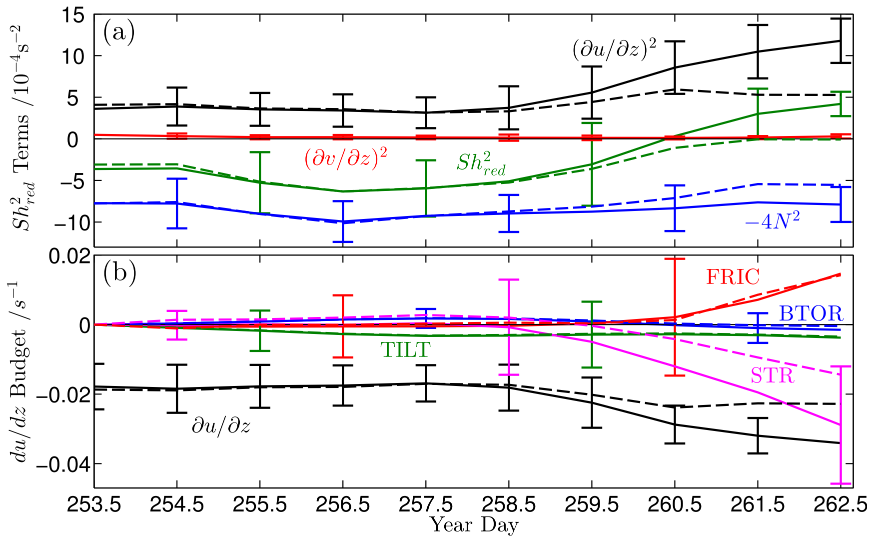

FIG. 6. (a) The evolution of the reduced shear squared $\mathrm{Sh}^2_{\mathrm{red}}$ and its components: the zonal shear squared $[(\partial u/\partial z)^2]$, meridional shear squared $[(\partial v/\partial z)^2]$, and −4 times the stratification $(-4N^2)$ following the particles shown in Fig. 5. (b) An analysis of diagnostics in the zonal shear $(\partial u/\partial z)$ budget [Eq. (4)] following the particles shown in Fig. 5. TILT denotes vortex tilting, STR denotes horizontal vortex stretching, FRIC denotes the frictional torque, and BTOR denotes the baroclinic torque. The error bars represent the $\pm 1\sigma$ spread over the particle ensemble, representing the spatial variability in the underlying fields over the span of the particles. The dashed lines in (a) and (b) are the equivalent curves obtained by first sorting every vertical profile in the simulations using the marginal stability adjustment algorithm described in the appendix and then taking finite-difference derivatives according to Eq. (4). The marginal stability–adjusted FRIC [red dashed curve in (b)] is calculated as a residual.

equator that acts on the existing shear of the EUC to increase it. Positive meridional diffluence driven by the horizontal flow of TIWs is present at the leading edge of the TIW warm phase [Fig. 1f; also see Fig. 3 of Perez et al. (2010)], in the same phase as the high $\mathrm{Sh}^2_{\mathrm{red}}$ (cf. Figs. 1f and 1g near the patches of high $\mathrm{Sh}^2_{\mathrm{red}}$). The correlation between $\partial v/\partial y$ and $\partial u/\partial z$ in the upper EUC shear layer at 0°, −140°E reaches a maximum at a lag of 2 days of −0.25 (significant at 95%), showing that maximum meridional diffluence leads minimum (maximum magnitude) zonal shear at 2 days. This is consistent with the pathway of Lagrangian fluid parcels in the EUC and the time-integrated nature of the vortex stretching term in Eq. (4), where meridional diffluence must act over time to increase the zonal shear. This is further illustrated with a Hovmöller diagram of the $\mathrm{Sh}^2_{\mathrm{red}}$ and meridional diffluence, which highlights the strong correspondence between the two variables, with most patches of high mixing preceded by meridional diffluence in longitude and time (Fig. 7).

Modulation of vertical mixing through horizontal vortex stretching does not require the horizontal circulation of TIWs to be divergent. While TIWs are associated with large-scale vertical motions [as discussed in Jochum and Murtugudde (2006) and Perez et al. (2010)], in our simulations most of the horizontal vortex stretching is a result of the component of the TIW velocity field that is horizontally nondivergent ($\partial u/\partial x + \partial v/\partial y \approx 0$). The physics of the mechanism are summarized in Fig. 8.

On the trailing edge of the TIW warm phase, TIW horizontal strain drives meridional confluence ($\partial v/\partial y < 0$) and thus horizontal vortex squashing. Because of the dependence of the vortex stretching on the zonal shear itself [STR in Eq. (4)], meridional confluence does not drive strong reductions in shear. While not the focus of this study, Lagrangian analyses show that patches of low $\mathrm{Sh}^2_{\mathrm{red}}$, and thus low turbulent mixing, can be partially attributed to restratification driven by TIW meridional shear acting on the north equatorial front (not shown). This TIW-driven periodic stratification, combined with the variations in mixing itself, may contribute to the variations in stratification at TIW frequencies seen in the Eulerian analysis (Fig. 3f). Furthermore, this emphasizes that the meridional shear of TIWs, while having a limited direct contribution to the $\mathrm{Sh}^2_{\mathrm{red}}$, plays a role in driving variations in stratification that influence mixing.

The nonlinear nature of horizontal vortex stretching, whereby vortex stretching drives large increases in shear while squashing drives lesser decreases in shear, suggests that TIWs may increase the average levels of turbulence in the upper EUC. This is examined in the following section.

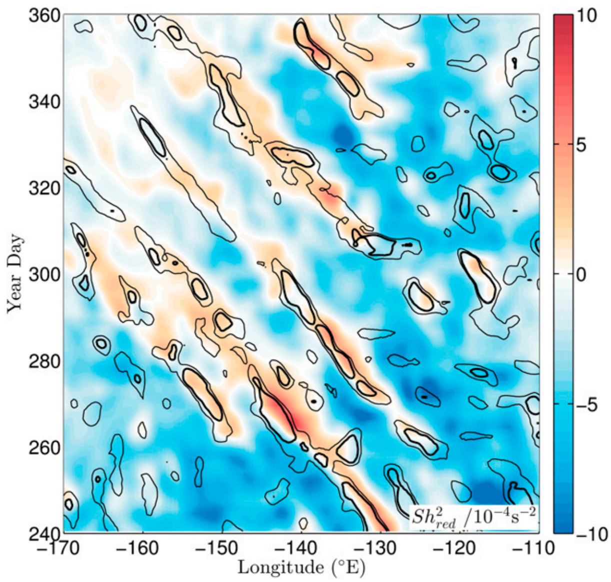

FIG. 7. Hovmöller plot of the reduced shear squared (color) and meridional diffluence ($\partial v/\partial y$, contours) at 72-m depth on the equator from the basinwide ROMS simulation. The x axis is longitude, and the y axis is time in yeardays for the months September–December. The thin (thick) contours denote where $\partial v/\partial y = 1 \times 10^{-6}\,\mathrm{s}^{-1}$ ($2 \times 10^{-6}\,\mathrm{s}^{-1}$). Note that positive meridional diffluence is often collocated or leads high $\mathrm{Sh}^2_{\mathrm{red}}$ patches, consistent with horizontal vortex stretching.

5. A simple mixing model of the EUC: TIW influence

This section discusses the total influence of the TIW modulation of the shear on the turbulent heat flux in the context of a simple 1D mixing model of the EUC forced by periodic TIW horizontal strain with alternating periods of meridional diffluence and confluence. We quantify this influence by comparing these 1D mixing model runs with and without TIW strain forcing.

a. 1D model setup

We split the zonal flow at 0°, −140°E into two parts associated with the EUC and TIWs, respectively:

$$u = \underbrace{\tilde{u}(z,t)}_{\text{EUC}} + \underbrace{u'(x,y,z,t)}_{\text{TIW}}, \tag{5}$$

where we assume that the TIW part is horizontally nondivergent and follows a simple 15-day sinusoidal oscillation

$$\frac{\partial v'}{\partial y} = -\frac{\partial u'}{\partial x} = \alpha(z,t) = A(z)\sin\left(\frac{2\pi t}{15\ \text{days}} + \phi_0\right), \tag{6}$$

where ϕ_0 represents the initial phase. The vertical shape function

$$A(z) = 2.8 \times 10^{-6}\,\mathrm{s}^{-1} + z \times 5.2 \times 10^{-9}\,\mathrm{m}^{-1}\,\mathrm{s}^{-1} \tag{7}$$

was chosen by fitting the RMS variations in $\partial v/\partial y$ in the TIW frequency band (calculated from the 3D ROMS model in a similar fashion to the profiles in Fig. 3) to a linear function in z. Although we do not have direct observations of $\partial v/\partial y$ to compare to Eq. (7), we would expect this fitted amplitude to be similar to observations, given that the 3D model TIW meridional velocity amplitude and $\partial v/\partial z$ amplitude (Fig. 3c) compare favorably

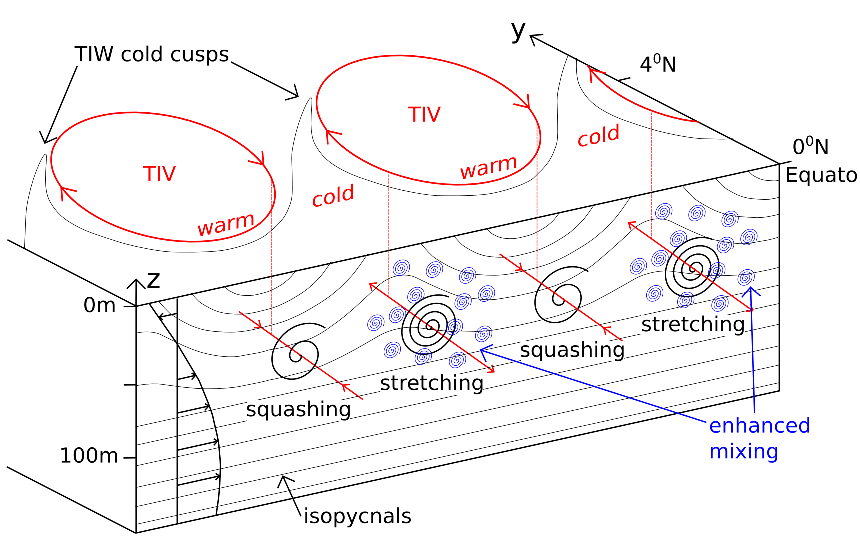

FIG. 8. A schematic showing how periodic strain driven by the TIW velocity field (red lines) acts on the horizontal vorticity of the EUC (indicated by the large black spirals) to increase or decrease the shear leading to patches of high (small blue spirals) and low turbulent mixing along the equator.

with observations, and the lateral structure of the 3D model TIWs is comparable to observations (Qiao and Weisberg 1995; Kennan and Flament 2000).

With the idealized TIWs, the zonal momentum equation for the EUC portion of the velocity field becomes

$$\frac{\partial \tilde{u}}{\partial t} = -\frac{\partial u'}{\partial x}\tilde{u} + \{\text{other advection terms}\} - \frac{1}{\rho_0}\frac{\partial \tilde{P}}{\partial x} + F_x, \tag{8}$$

where F_x represents a frictional force associated with vertical mixing and surface forcing, and $\tilde{P}$ is the pressure associated with the EUC portion of the flow. We assume that the advection terms in the curly brackets can be treated as external forcing in this 1D framework and can be included as part of a large-scale forcing term PA. This term represents the pressure gradient and advective processes that maintain the EUC against vertical mixing and was chosen to balance the wind stress over the total water column. It has a cubic Gaussian shape

$$PA = -\frac{\tau_x}{\rho_0}\exp[(z/d)^3]\left[\int_{-\infty}^{0}\exp[(z'/d)^3]\,dz'\right]^{-1}, \tag{9}$$

with decay scale $d = 120$ m, chosen as it matched the form of the 3D model pressure gradient well.

Dropping the ~ from Eq. (8), the above approximations result in a simple 1D diffusion equation model for the EUC velocity $u(z, t)$, where we also include equations for the temperature $T(z, t)$ and salinity $S(z, t)$:

$$\frac{\partial u}{\partial t} = \underbrace{\alpha(z,t)u}_{\text{TIW Strain}} + \underbrace{PA}_{\text{Pressure/Adv.}} \underbrace{-\frac{\partial}{\partial z}\left(-\kappa_v\frac{\partial u}{\partial z}\right)}_{\text{Diffusion}}, \quad \text{and} \tag{10}$$

$$\frac{\partial\{T,S\}}{\partial t} = \underbrace{-\frac{1}{r_T}\{T-T_0, S-S_0\}}_{\text{Restoring}} \underbrace{-\frac{\partial}{\partial z}\left(-\kappa_T\frac{\partial\{T,S\}}{\partial z}\right)}_{\text{Diffusion}}, \tag{11}$$

where the first (second) member of the curly brackets is taken for the temperature (salinity) equation. The Newtonian restoring added to the temperature and salinity equations represents the pressures that maintain the stratification against vertical mixing. The main results are not very sensitive to values of the restoring time scale between 1 and 15 days (not shown), and thus $r_T = 5$ days was chosen. We solve these equations on the same 50-level vertical grid as the 3D ROMS model.

The surface forcing at 0°N, −140°E averaged over the TIW season (September–December) from the 3D ROMS model was used to force the 1D model, including a $\tau_x = -0.08\,\mathrm{N\,m^{-2}}$ zonal wind stress, a free-slip bottom boundary condition, a downward shortwave radiative heat flux of $275\,\mathrm{W\,m^{-2}}$, and a combined sensible plus latent heat flux of $-180\,\mathrm{W\,m^{-2}}$. We found that including a diurnal cycle of shortwave radiation did not significantly change the results discussed here and thus for simplicity we discuss only model runs without a diurnal cycle.

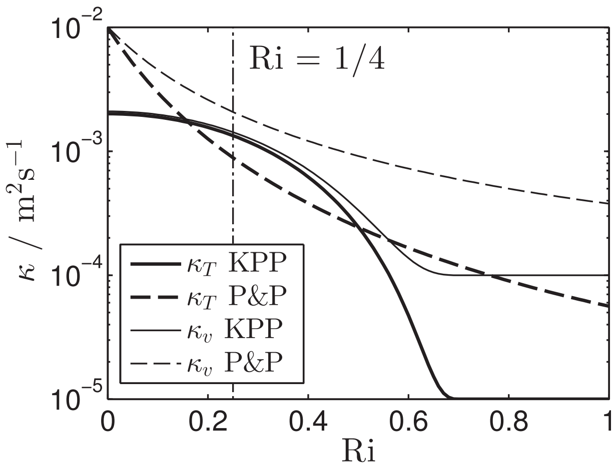

FIG. 9. The interior diffusivities (κ_T) and viscosities (κ_v) assigned by the KPP (Large et al. 1994) and P&P (Pacanowski and Philander 1981) interior mixing schemes for shear instability as a function of the gradient Richardson number [as in Eqs. (13)–(16)].

We compare the results of simulations using two parameterizations for the diffusion terms in Eqs. (10) and (11). The diffusivity and viscosity in both schemes are split into components above and below the boundary layer depth (H_{BL}):

$$\kappa = \begin{cases}\kappa_{BL}, & z > -H_{BL},\\ \kappa_{int}, & z \le -H_{BL},\end{cases} \tag{12}$$

where the boundary layer depth and boundary layer diffusivity/viscosity κ_{BL} are determined in both schemes by the KPP boundary layer model of Large et al. (1994). However, the schemes differ in the interior parameterization for the diffusivity/viscosity κ_{int}, with the first scheme (the KPP scheme) using the KPP interior form used in the 3D ROMS model (Large et al. 1994):

$$\kappa_v = K_0\left[1-\left(\frac{\mathrm{Ri}}{\mathrm{Ri}_0}\right)^2\right]^3 + \kappa_{vB}, \quad \text{and} \tag{13}$$

$$\kappa_T = K_0\left[1-\left(\frac{\mathrm{Ri}}{\mathrm{Ri}_0}\right)^2\right]^3 + \kappa_{TB}, \tag{14}$$

where κ_v is the viscosity, κ_T is the diffusivity for scalars, $K_0 = 2\times10^{-3}\,\mathrm{m^2\,s^{-1}}$, $\mathrm{Ri}_0 = 0.7$, and the background

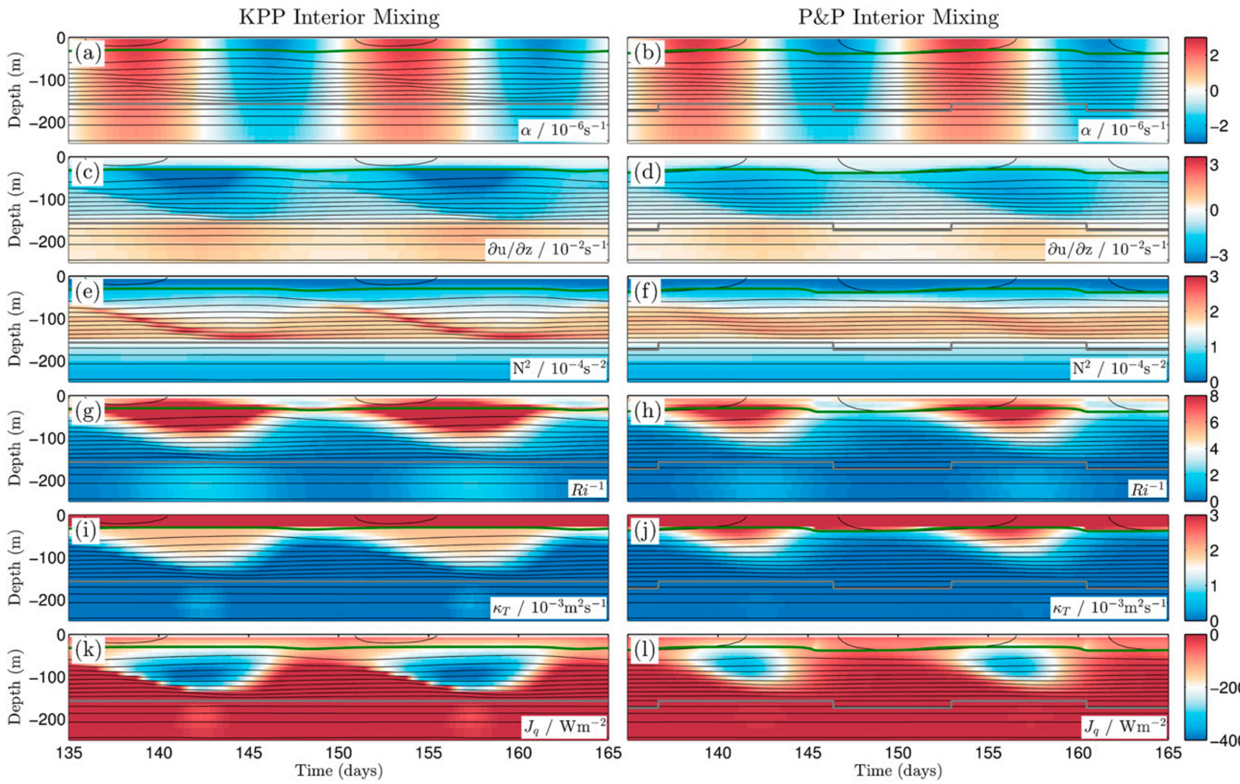

FIG. 10. Time–depth plots of simple 1D mixing model runs using (left) KPP and (right) P&P over days 135–165. The (a),(b) imposed TIW periodic strain, (c),(d) zonal shear, (e),(f) stratification, (g),(h) inverse Richardson number, (i),(j) diffusivity, and (k),(l) vertical turbulent heat flux. The dark green lines indicate the depth of the KPP mixed layer, the gray lines indicate the depth of the EUC core, and the black contours are isopycnals at 0.2 kg m^{-3} spacing.

diffusivities are $\kappa_{TB} = 1\times10^{-5}\,\mathrm{m^2\,s^{-1}}$ and $\kappa_{\nu B} = 1\times10^{-4}\,\mathrm{m^2\,s^{-1}}$ (Fig. 9). These parameters are consistent with previous parameter choices for this scheme (Large et al. 1994; Large and Gent 1999; Zaron and Moum 2009). The K_0 parameter is smaller than values used elsewhere and was chosen as it gave the most appropriate mean EUC depth in the 3D ROMS model as determined by a sensitivity study (not shown).

The second scheme replaces κ_{int} with the form of Pacanowski and Philander (1981) (we refer to this scheme as the P&P scheme):

$$\kappa_\nu^{\mathrm{PP}} = K_0^{\mathrm{PP}}\left(1+\frac{\mathrm{Ri}}{\mathrm{Ri}_0^{\mathrm{PP}}}\right)^{-2} + \kappa_{\nu B}, \quad \text{and} \tag{15}$$

$$\kappa_T^{\mathrm{PP}} = \kappa_\nu^{\mathrm{PP}}\left(1+\frac{\mathrm{Ri}}{\mathrm{Ri}_0^{\mathrm{PP}}}\right)^{-1} + \kappa_{sB}, \tag{16}$$

where $K_0^{\mathrm{PP}} = 0.01\,\mathrm{m^2\,s^{-1}}$ and $\mathrm{Ri}_0^{\mathrm{PP}} = 0.2$. These parameters are consistent with previously cited values (e.g., Pacanowski and Philander 1981; Blanke and Delecluse 1993; Li et al. 2001). The P&P parameterization should be more successful at enforcing marginal stability than the KPP parameterization, as it has a steeper increase in diffusivity as the Richardson number passes ¼ and thus can provide relatively more mixing at low Richardson numbers (Fig. 9). At low Richardson numbers the P&P scheme has a Prandtl number greater than 1 unlike KPP and thus preferentially mixes momentum over buoyancy to more efficiently increase the Richardson number. At high Richardson numbers both schemes have Prandtl numbers greater than 1.

The simple 1D mixing model runs were initialized with the 3D ROMS model profiles at 0°, −140°E averaged over the TIW season (September–December) and run for 200 days. We choose the tenth TIW period between days 135 and 150 for our analysis because by this time the results are not sensitive to the initial phase ϕ_0 of the strain α.

The simple 1D model shows similar qualitative results to the 3D ROMS model. During periods when $\alpha(z, t) > 0$ (Figs. 10a,b), the zonal shear increases, peaking in magnitude 3–4 days after the maximum strain (Figs. 10c,d). High zonal shear is accompanied by low Richardson numbers (Figs. 10g,h), resulting in large diffusivities (Figs. 10i,j) that mix out the stratification

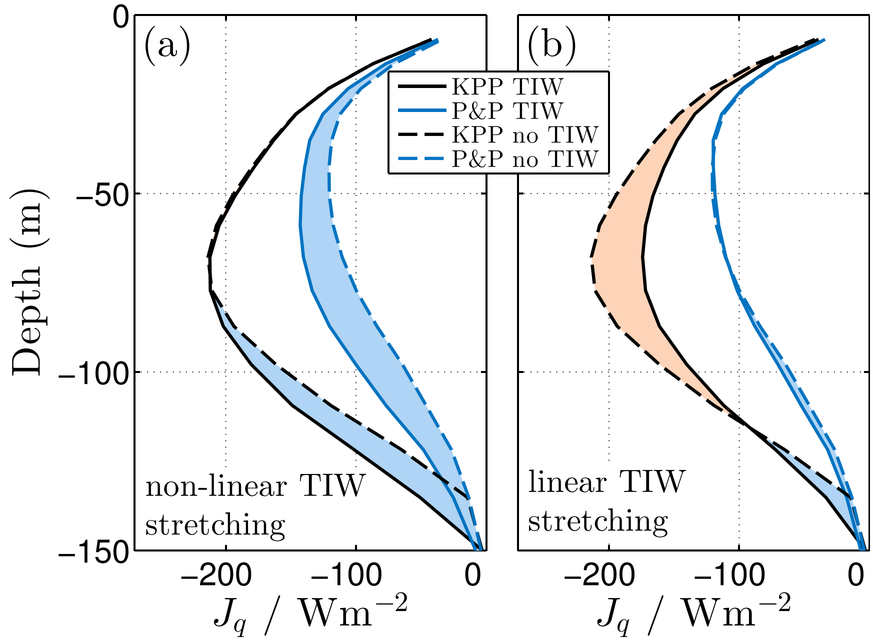

FIG. 11. The vertical turbulent heat flux [J_q, Eq. (17)] averaged over days 135–150 for simple mixing model runs with [$\alpha(z, t)$ as in Eq. (6); solid lines] and without [$\alpha(z, t) = 0$; dashed lines] TIWs. Shown are (a) runs with nonlinear TIW stretching, where the TIW body force depends on the velocity itself $\alpha(z, t)u(z, t)$, and (b) linear TIW stretching, where the TIW body force depends on a mean velocity $\alpha(z, t)\overline{u}(z)$. Areas are shaded according to whether adding TIWs increases (blue) or decreases (orange) the turbulent heat flux averaged over a TIW period. Adding nonlinear TIW stretching increases the turbulent heat flux in all cases with the magnitude of the increase depending on the parameterization for shear instability used.

(Figs. 10e,f) through the divergence of the turbulent heat flux (Figs. 10k,l):

$$J_q = -C_p\rho_0\kappa_T\frac{\partial T}{\partial z}, \tag{17}$$

where C_p is the specific heat of seawater. As the TIW strain switches sign to become negative ($\alpha < 0$ in Figs. 10a,b), the shear is reduced both through vortex squashing and as a result of the mixing itself. The T-S restoring and the surface heat fluxes then act to restore the stratification profile before the TIW strain switches sign and a new phase of increased mixing begins.

In these simple 1D mixing model simulations, the P&P scheme does a better job at enforcing marginal stability than KPP, restricting the Richardson number to larger values (cf. Figs. 10g and 10h). The P&P diffusivity is able to reach higher values when the Richardson number is low (cf. Figs. 10i and 10j) and preferentially mixes momentum over buoyancy when the Prandtl number is greater than 1. This results in lower maximum turbulent heat fluxes for P&P compared to KPP (cf. Figs. 10k to 10l). The turbulent heat fluxes averaged over a TIW period (Fig. 11) are also lower for P&P compared to KPP (cf. black and blue lines in Fig. 11a) for model runs both with periodic TIW strain [$\alpha(z, t)$ as in Eq. (6); solid lines in Fig. 11a] and runs without TIW periodic strain [$\alpha(z, t)$ set to zero; dashed lines in Fig. 11a].

b. The influence of TIWs on the turbulent heat flux

Inclusion of TIW periodic strain results in an increase in the magnitude of the turbulent heat flux averaged over a TIW period (Fig. 11a). The increase is restricted to depths below 75 m for the KPP simulation (cf. black solid and dashed curves in Fig. 11a), while for P&P, the heat flux increases at all depths (cf. blue solid and dashed curves in Fig. 11a). The rectified change in turbulent heat flux R at a given depth is defined as

$$\begin{aligned} R &\equiv \overline{J_q(t)} - \overline{J_q}^n \\ &= -\rho_0 c_p\left[\overline{\kappa(\mathrm{Ri})\frac{\partial T}{\partial z}} - \kappa(\overline{\mathrm{Ri}}^n)\overline{\frac{\partial T}{\partial z}}^n\right], \end{aligned} \tag{18}$$

where the overbar represents an average over a TIW period, and overbar^n represents an equivalent average in the run without TIWs. There are a number of

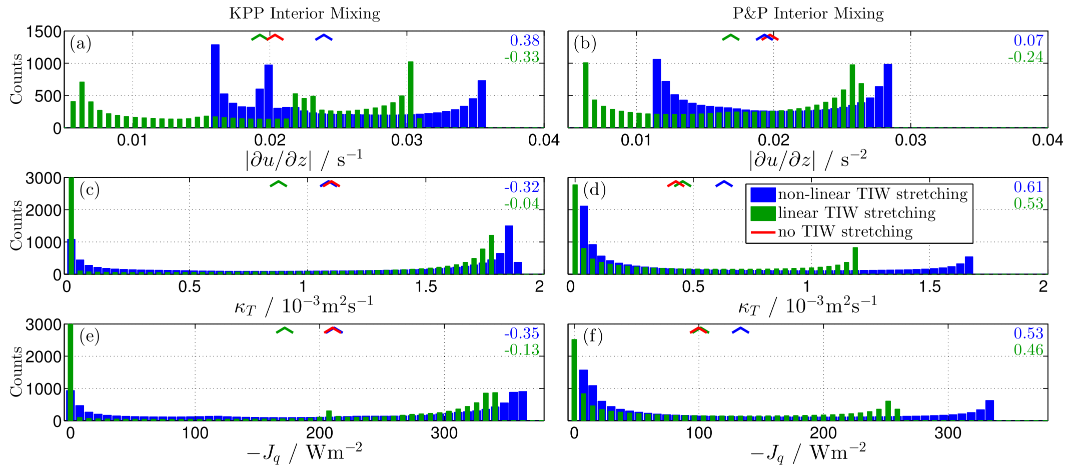

FIG. 12. Histograms of the magnitude of the (a),(b) zonal shear, (c),(d) diffusivity, and (e),(f) turbulent heat flux over a TIW period at 75-m depth for simple 1D mixing model runs with the (left) KPP and (right) P&P mixing schemes. The blue (green) histograms show the results of runs with nonlinear (linear) TIW stretching. The distribution means are indicated with arrows at the top of the figures, including the mean for runs without TIWs (red arrows). The skew of each distribution is indicated in the upper right of each panel. The distribution of negative turbulent heat flux is plotted to facilitate comparison with the diffusivity distributions.

nonlinearities in the system that are potentially responsible for rectification $R \neq 0$:

1) the influence of variations in stratification, both through the dependence of the Richardson number on stratification $[\mathrm{Ri} = N^2/(\partial u/\partial z)^2]$ and the dependence of the heat flux on the product of the diffusivity and the vertical temperature gradient $(\overline{\kappa \partial T/\partial z} \neq \overline{\kappa}\, \overline{\partial T/\partial z})$;
2) the nonlinear dependence of the diffusivity on the Richardson number and through it on the shear, which differs between the two mixing schemes $[\overline{\kappa(\mathrm{Ri})} \neq \kappa(\overline{\mathrm{Ri}})]$;
3) the influence of mixing on the underlying shear distribution [even if the diffusivity depends linearly on the shear (i.e., removing nonlinearity 2), the mixing acts preferentially at high shears and thus can result in rectification $(\overline{\partial u/\partial z} \neq \overline{\partial u/\partial z}^n)$]; and
4) the nonlinear influence of vortex stretching on the shear $(\overline{\partial u/\partial z} \neq \overline{\partial u/\partial z}^n)$.

The influence of temporal variations in stratification and the temperature gradient on the heat flux (nonlinearity 1) is minimal. While the vertical gradient in stratification is large, its temporal variations are weaker than the corresponding variations in shear (cf. Figs. 10e,f with Figs. 10c,d) and thus do not have a strong influence on the temporal variations in the Richardson number (cf. Figs. 10e,f with Figs. 10g,h). In addition, dT/dz averaged over a TIW period is similar to dT/dz from the no TIW runs (not shown), and the distribution over a TIW period of the turbulent heat flux at a fixed depth matches the distribution of diffusivity closely (cf. blue distributions in Figs. 12e,f to Figs. 12c,d), implying minimal influence by variations in dT/dz.

The nonlinear dependence of the KPP and P&P diffusivity on the Richardson number and shear (nonlinearity 2) has a strong influence on the turbulent heat flux averaged over a TIW period and is responsible for the differences between the two mixing schemes. Given that variations in stratification are minimal, this nonlinearity is well captured by considering the dependence of the diffusivity on the shear at an average value of the stratification for each mixing scheme (Fig. 13). Using a Taylor series expansion of the functional dependence of the diffusivity on the shear $G = \kappa(\partial u/\partial z)$, about the shear averaged over a TIW period $\overline{\partial u/\partial z}$, it can be shown that to first order in the shear oscillation variance $\mathrm{var}(\partial u/\partial z)$

$$R_\kappa \equiv \overline{G} - G\left(\frac{\overline{\partial u}}{\partial z}\right) \approx \frac{1}{2}G''\mathrm{var}\left(\frac{\partial u}{\partial z}\right), \qquad (19)$$

where R_κ is the rectification effect of this nonlinearity, and G'' is the curvature of G. Thus, as a consequence of the positive curvature of the P&P curve (Fig. 13), the distribution of P&P diffusivity over a TIW period at an example depth is positively skewed (0.61 at 75 m; blue distribution in Fig. 12d), resulting in a positive rectification effect $R_\kappa > 0$ (cf. no TIW to nonlinear TIW means in Fig. 12d). On the other hand, the negative curvature

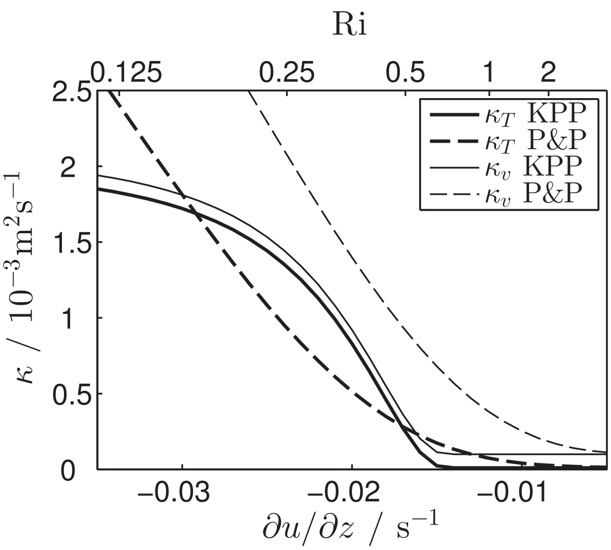

FIG. 13. The KPP and P&P interior diffusivities (κ_T) and viscosities (κ_ν) as a function of the shear $\partial u/\partial z$ for a stratification of $N^2 = 1.42 \times 10^{-4}\,\mathrm{s}^{-2}$, close to the stratification at 75 m averaged over the period shown in Fig. 5 for both the KPP ($N^2 = 1.37 \times 10^{-4}\,\mathrm{s}^{-2}$) and P&P ($N^2 = 1.47 \times 10^{-4}\,\mathrm{s}^{-2}$) runs. The corresponding values of the Richardson number are shown on the top axis. A linear diffusivity scale is used to highlight the different curvatures of the two schemes.

of the KPP curve (Fig. 13) results in a negatively skewed KPP diffusivity distribution over a TIW period (−0.32 at 75 m; blue distribution in Fig. 12c) and would tend to result in a negative rectification effect. However, the total rectification R is also influenced by the other two nonlinearities, the influence of the mixing on the shear distribution (nonlinearity 3) and the nonlinearity in vortex stretching (nonlinearity 4), that can cause differences between the shear averaged over a TIW period and the shear for the no TIW run ($\overline{\partial u/\partial z} \neq \overline{\partial u/\partial z}^{n}$) and influence the oscillation amplitude [var($\partial u/\partial z$)].

Nonlinearities 3 and 4 have counteracting influences on the shear distribution. The mixing preferentially acts at high shear (for both mixing schemes), tending to negatively skew the shear magnitude distribution and result in a rectified decrease in the shear magnitude averaged over a TIW period compared to runs without TIWs. The nonlinearity of vortex stretching induces stronger vortex stretching at high shears, positively skewing the shear magnitude distribution and resulting in a rectified increase in the shear magnitude averaged over a TIW period compared to runs without TIWs. For P&P, the skew of the shear magnitude distribution is small (0.07; blue distribution in Fig. 12b) and so is the rectified change in mean shear magnitude (cf. no TIW to nonlinear TIW means in Fig. 12b), suggesting that mixing and vortex stretching compensate. While for KPP, the skew of the shear magnitude distribution is positive (0.38; blue distribution in Fig. 12a), and the rectified change in mean shear magnitude is positive (cf. no TIW to nonlinear TIW means in Fig. 12a), suggesting that the vortex stretching nonlinearity overpowers the mixing nonlinearity for KPP. However, interpreting the impact of nonlinearities 3 and 4 on the heat fluxes based solely on these qualitative arguments is potentially misleading as they can interact with each other and with nonlinearity 2 associated with the curvature in G.

To quantitatively evaluate the importance of the vortex stretching nonlinearity compared to the other nonlinearities 1–3, we replace the regular nonlinear TIW stretching [$\alpha(z, t)u(z, t)$ in Eq. (10)] with linear TIW stretching [$\alpha(z, t)\overline{u}(z)$, where $\overline{u}(z)$ was the mean velocity profile between days 135 and 150 from the simulations with nonlinear TIW stretching]. In simulations performed with linear TIW stretching, the TIW body force no longer depends on the magnitude of the instantaneous velocity, and thus without mixing a simple symmetric sinusoidal oscillation in shear at each depth would result. Indeed, in these linear runs, the skew of the shear magnitude distributions becomes negative as a result of the mixing nonlinearity 3 (cf. the skews of the blue and green distributions in Figs. 12a and 12b). These changes result in modifications to the distributions of the diffusivity and the turbulent heat flux (cf. blue and green distributions in Figs. 12c–f). In particular, the turbulent heat flux averaged over a TIW period in simulations with linear TIW stretching is now reduced in comparison to the nonlinear TIW stretching runs (cf. Figs. 11a and 11b). For KPP, linear TIW stretching results in a rectified decrease in the heat flux, as a consequence of both the negative curvature of the KPP G curve (Fig. 13) and the mixing nonlinearities. For P&P, the linear TIW stretching results in no change in the average turbulent heat flux compared to simulations without TIWs, likely as a result of the cancellation between the mixing nonlinearity and the nonlinearity associated with the positive curvature of the P&P G curve (Fig. 13). These results emphasize that the dependence of horizontal vortex stretching on the shear itself is the critical nonlinearity that gives rise to the rectified increase in turbulent heat flux $R > 0$ when TIWs are added.

In the context of this simple 1D mixing model for the EUC, TIWs increase the turbulent heat flux averaged over a TIW period through horizontal vortex stretching. Averages of J_q between 50 and 100 m (Table 1), indicative of the total change in heat content induced by turbulent mixing between this depth layer and the surface, show that TIWs cool the upper ocean in both parameterizations examined here. However, the magnitude of the cooling varies between parameterizations. Using

TABLE 1. Turbulent heat flux J_q (W m^{-2}) averaged over days 135–165 between 50 and 100 m from the simple 1D mixing model runs.

Interior scheme	K_0 (m^2 s^{-1})	Ri_0	K_0^{PP}(m^2 s^{-1})	J_q without TIWs	J_q with TIWs	% increase
KPP	2×10^{-3}	0.7	—	−197	−201	2
KPP	4×10^{-3}	0.7	—	−231	−248	7
KPP	2×10^{-3}	0.8	—	−206	−210	2
P&P	—	—	1×10^{-2}	−98	−129	32
P&P	—	—	5×10^{-3}	−100	−127	27
Peters et al. (1988)	—	—	—	−71	−100	41

the P&P parameterization, which more realistically enforces marginal stability, TIWs increase the turbulent heat flux averaged between 50 and 100 m by 30%. Runs conducted using the κ(Ri) curves of Peters et al. (1988), which have very rapid increases in diffusivity as the Richardson number decreases below 1/4, show a further enhancement of the turbulent heat flux by TIWs to 40% (Table 1). This suggests that the rectified TIW influence is larger for parameterizations that are more successful at enforcing marginal stability and whose diffusivity formulas are more consistent with observations.

While the details of the simple 1D mixing runs are sensitive to the parameters in the mixing schemes, the influence of TIWs on the heat flux is not sensitive to these parameters, only to the shape and curvature of the κ(Ri) curve. Sensitivity studies where the KPP maximum diffusivity K_0 was doubled to 4×10^{-3} m^2 s^{-1} (as in Large and Gent 1999), the KPP critical Richardson number Ri_0 was changed to 0.8 (as in Large and Gent 1999), and the P&P maximum diffusivity K_0^{PP} was halved to 5×10^{-3} m^2 s^{-1} (as in Ma et al. 1994) show only small changes to the influence of TIWs on the turbulent heat flux (Table 1).

6. Summary and discussion

Recent observations (Lien et al. 2008; Moum et al. 2009; Inoue et al. 2012) have shown that TIWs modulate vertical mixing in the upper EUC, with potential implications for the role of TIWs in the equatorial SST budget. Using a regional ocean model, we have examined the mechanisms through which TIWs modulate the $\mathrm{Sh}^2_{\mathrm{red}}$, a proxy for mixing. Contrary to previous hypotheses, our results suggest that the varying TIW meridional shear plays a minor direct role in modulations of mixing (Fig. 3c). Instead, we find that TIW horizontal strain modifies the zonal shear of the upper EUC through horizontal vortex stretching (Fig. 8), acting to increase vertical mixing leading into the TIW warm phase. By including the effects of TIW horizontal strain in a simple 1D mixing model of the EUC, we further showed that adding TIWs can result in a rectified increase in the turbulent heat flux and thus sea surface cooling in this simple context. The amount of sea surface cooling induced by TIWs is larger for parameterizations that are more successful at enforcing the observed (Smyth and Moum 2013) physical constraint of marginal stability. This result has potential implications for the SST budget in ocean models using Richardson number–based mixing parameterizations, such as many of the phase 5 of CMIP (CMIP5) ocean models (Huang et al. 2014).

Horizontal vortex stretching here relies on TIW horizontal strain interacting with the vertical shear in the upper EUC. This coupling of vertical and horizontal processes is a signature of submesoscale physics, which have been found previously to play a role in the dynamics of TIWs and TIVs (Holmes et al. 2014). MacDonald and Chen (2012) found that a similar mechanism involving lateral spreading at a river outlet was important in enhancing stratified shear turbulence in a coastal scale flow. The meridional diffluence that drives vortex stretching acts frontolytically on the equatorial fronts to decrease the horizontal buoyancy gradient. However, the constraint of thermal wind balance is weakened near the equator where the Coriolis parameter is weak. The tilting of planetary and relative vorticity that would normally act (in the midlatitudes) to decrease the shear and maintain thermal wind balance in response to the decreasing horizontal buoyancy gradient does not act strongly here. Thus, this process is distinctly different from the frontogenetic intensification of shear and turbulence discussed by Skyllingstad and Samelson (2012).

In the context of a simple 1D mixing model of the EUC, TIWs increased the turbulent heat flux by $\sim$30 W m^{-2} (Fig. 11a; Table 1), which is of similar magnitude to the TIW lateral heat fluxes estimated in Jochum and Murtugudde (2006). For a 30-m-deep mixed layer, this additional heat flux drives an additional cooling of -0.6°C month^{-1}, a significant fraction of the 1°–2°C month^{-1} cooling implied by the turbulent heat flux observations of Moum et al. (2009) and comparable to the $O(1)$°C month^{-1} TIW lateral heating rate (Menkes et al. 2006; Jochum et al. 2007). Thus, the additional mixing-induced cooling effect of TIWs could potentially compensate for TIW lateral heating. However, this result must be considered with caution given the simplified nature of the 1D mixing model and the parameterized mixing.

We have not considered here any rectified influence of TIWs on the surface heat fluxes. The studies of Thum et al. (2002) and Seo et al. (2007) found variations in the latent heat flux of $\sim 50\,\mathrm{W\,m^{-2}\,(^{\circ}C)^{-1}}$ of TIW-induced SST change, with the sensible heat flux changes being significantly smaller. Seo et al. (2007) showed that the rectified influence of these changes averaged over a TIW period was negligible ($<1\,\mathrm{W\,m^{-2}}$), and thus we expect the increase in turbulent heat flux due to TIWs to dominate any TIW-induced changes in air–sea fluxes.

Our results, combined with the study of Zaron and Moum (2009), suggest that there are several improvements that could be made to the interior KPP mixing parameterization scheme to better model the equatorial oceans and the influence of TIWs on vertical mixing. The inclusion of the KPP boundary layer scheme has been shown to significantly improve simulations of the tropical Pacific compared to the original Pacanowski and Philander (1981) scheme (Li et al. 2001). Our modeling work and observations of $\kappa(\mathrm{Ri})$ curves (i.e., Fig. 1 of Zaron and Moum 2009) suggest that using the interior schemes of Pacanowski and Philander (1981) or Peters et al. (1988) combined with the KPP boundary layer model (Large et al. 1994) may perform better than the original KPP scheme with respect to enforcing marginal stability and thus modeling the influence of TIWs on vertical mixing. This type of scheme has been used in the HadCM3 climate model (Gordon et al. 2000), although the authors did not discuss the reasons for this choice. However, in any future vertical mixing sensitivity study, it must be noted that the strength of TIWs themselves is influenced by vertical mixing, rendering the interpretation of results difficult (Chen et al. 1994).

Acknowledgments. We thank J. Moum for useful discussions. The computations were performed at the Stanford Center for Computational Earth and Environmental Science. We thank the TAO Project Office of NOAA/PMEL for providing the TAO data. R. Holmes was supported by a Stanford Graduate Fellowship while undertaking this study.

APPENDIX

Marginal Stability Adjustment Algorithm

The algorithm described here is similar to the Price et al. (1986) mixing scheme but acts offline as a diagnostic tool. Given some initial profiles of velocities $u^I(z)$ and $v^I(z)$, potential temperature $T^I(z)$, salinity $S^I(z)$, and buoyancy $b^I(z)$, we wish to find sorted profiles $u(z)$, $v(z)$, $T(z)$, $S(z)$, and $b(z)$ that are stable or marginally stable throughout the water column ($\mathrm{Sh}^2_{\mathrm{red}} \le 0$), subject to conservation of momentum, heat, and salt. To satisfy these conditions, we construct an algorithm that induces downgradient fluxes of momentum, heat, and salt iteratively at each unstable vertical grid point ($\mathrm{Sh}^2_{\mathrm{red}} > 0$) in the profile until that point is marginally stable ($\mathrm{Sh}^2_{\mathrm{red}} = 0$). At each iteration the fluxes are imposed at a Prandtl number one ratio, and the flux formulation conserves momentum, heat, and salt by construction. For each vertical profile, the algorithm proceeds as follows:

1) Homogenize regions with negative stratification: while [$N^2(z) < 0$ at some z]
   (i) find block of grid points with $N^2(z) < 0$;
   (ii) homogenize $u(z)$, $v(z)$, $T(z)$, and $S(z)$ within this block conserving total momentum, heat and salt within block; and
   (iii) recalculate $N^2(z)$ everywhere.
2) Enforce marginal stability at unstable grid points: while ($\mathrm{Sh}^2_{\mathrm{red}} > 0$ at some z)
   (i) find grid point k with maximum $\mathrm{Sh}^2_{\mathrm{red}}$;
   (ii) apply downgradient fluxes of momentum, heat, and salt at this grid point, with the same effective diffusivity $\kappa_v = \kappa_T = \kappa_S$, until $\mathrm{Sh}^2_{\mathrm{red}}(k) = 0$; and
   (iii) recalculate $\mathrm{Sh}^2_{\mathrm{red}}$ everywhere.

An example calculation is shown in Fig. 4. In the second while loop, the applied fluxes result in reduced stratification and shear at the grid point of interest but increased shear and stratification at the neighboring grid points. As the algorithm continues, these high gradients are expelled from the unstable region. The resulting profiles have lower shear and stratification in the now marginally stable region (Figs. 4d,e,f between 80 and 40 m) and increased shear and stratification on the edges of the marginally stable region (Figs. 4d,e,f, between 110 and 80 m and above 40 m).

REFERENCES

An, S., 2008: Interannual variations of the tropical ocean instability wave and ENSO. *J. Climate,* **21,** 3680–3686, doi:10.1175/2008JCLI1701.1.

Bernie, D., S. Woolnough, J. Slingo, and E. Guilyardi, 2005: Modeling diurnal and intraseasonal variability of the ocean mixed layer. *J. Climate,* **18,** 1190–1202, doi:10.1175/JCLI3319.1.

——, E. Guilyardi, G. Madec, J. Slingo, and S. Woolnough, 2007: Impact of resolving the diurnal cycle in an ocean–atmosphere GCM. Part 1: A diurnally forced OGCM. *Climate Dyn.,* **29,** 575–590, doi:10.1007/s00382-007-0249-6.

Blanke, B., and P. Delecluse, 1993: Variability of the tropical Atlantic Ocean simulated by a general circulation model with two different mixed-layer physics. *J. Phys. Oceanogr.,* **23,** 1363–1388, doi:10.1175/1520-0485(1993)023<1363:VOTTAO>2.0.CO;2.

Chen, D., L. Rothstein, and A. Busalacchi, 1994: A hybrid vertical mixing scheme and its application to tropical ocean models. *J. Phys. Oceanogr.,* **24,** 2156–2179, doi:10.1175/1520-0485(1994)024<2156:AHVMSA>2.0.CO;2.

Chi, N.-H., R.-C. Lien, E. D'Asaro, and B. Ma, 2014: The surface mixed layer heat budget from mooring observations in the central Indian Ocean during Madden–Julian oscillation events. *J. Geophys. Res. Oceans,* **119,** 4638–4652, doi:10.1002/2014JC010192.

Contreras, R., 2002: Long-term observations of tropical instability waves. *J. Phys. Oceanogr.,* **32,** 2715–2722, doi:10.1175/1520-0485-32.9.2715.

Cox, M., 1980: Generation and propagation of 30-day waves in a numerical model of the Pacific. *J. Phys. Oceanogr.,* **10,** 1168–1186, doi:10.1175/1520-0485(1980)010<1168:GAPODW>2.0.CO;2.

Danabasoglu, G., W. Large, J. Tribbia, P. Gent, B. Briegleb, and J. McWilliams, 2006: Diurnal coupling in the tropical oceans of CCSM3. *J. Climate,* **19,** 2347–2365, doi:10.1175/JCLI3739.1.

Gordon, C., C. Cooper, C. Senior, H. Banks, J. Gregory, T. Johns, J. Mitchell, and R. Wood, 2000: The simulation of SST, sea ice extents and ocean heat transports in a version of the Hadley Centre coupled model without flux adjustments. *Climate Dyn.,* **16,** 147–168, doi:10.1007/s003820050010.

Graham, T., 2014: The importance of eddy permitting model resolution for simulation of the heat budget of tropical instability waves. *Ocean Modell.,* **79,** 21–32, doi:10.1016/j.ocemod.2014.04.005.

Holmes, R., L. Thomas, L. Thompson, and D. Darr, 2014: Potential vorticity dynamics of tropical instability vortices. *J. Phys. Oceanogr.,* **44,** 995–1011, doi:10.1175/JPO-D-13-0157.1.

Holzer, M., and E. Siggia, 1994: Turbulent mixing of a passive scalar. *Phys. Fluids,* **6,** 1820–1837, doi:10.1063/1.868243.

Huang, C., F. Qiao, and D. Dai, 2014: Evaluating CMIP5 simulations of mixed layer depth during summer. *J. Geophys. Res. Oceans,* **119,** 2568–2582, doi:10.1002/2013JC009535.

Imada, Y., and M. Kimoto, 2012: Parameterization of tropical instability waves and examination of their impact on ENSO characteristics. *J. Climate,* **25,** 4568–4581, doi:10.1175/JCLI-D-11-00233.1.

Inoue, R., R.-C. Lien, and J. Moum, 2012: Modulation of equatorial turbulence by a tropical instability wave. *J. Geophys. Res.,* **117,** C10009, doi:10.1029/2011JC007767.

Jing, Z., L. Wu, D. Wu, and B. Qiu, 2014: Enhanced 2-h–8-day oscillations associated with tropical instability waves. *J. Phys. Oceanogr.,* **44,** 1908–1918, doi:10.1175/JPO-D-13-0189.1.

Jochum, M., and R. Murtugudde, 2006: Temperature advection by tropical instability waves. *J. Phys. Oceanogr.,* **36,** 592–605, doi:10.1175/JPO2870.1.

——, M. Cronin, W. Kessler, and D. Shea, 2007: Observed horizontal temperature advection by tropical instability waves. *Geophys. Res. Lett.,* **34,** L09604, doi:10.1029/2007GL029416.

Kawai, Y., and A. Wada, 2007: Diurnal sea surface temperature variation and its impact on the atmosphere and ocean: A review. *J. Oceanogr.,* **63,** 721–744, doi:10.1007/s10872-007-0063-0.

Kennan, S., and P. Flament, 2000: Observations of a tropical instability vortex. *J. Phys. Oceanogr.,* **30,** 2277–2301, doi:10.1175/1520-0485(2000)030<2277:OOATIV>2.0.CO;2.

Large, W., and P. Gent, 1999: Validation of vertical mixing in an equatorial ocean model using large eddy simulations and observations. *J. Phys. Oceanogr.,* **29,** 449–464, doi:10.1175/1520-0485(1999)029<0449:VOVMIA>2.0.CO;2.

——, and S. Yeager, 2004: Diurnal to decadal global forcing for ocean and sea-ice models: The data sets and flux climatologies. NCAR Tech. Note NCAR/TN-460+STR, 105 pp., doi:10.5065/D6KK98Q6.

——, J. McWilliams, and S. Doney, 1994: Oceanic vertical mixing: A review and a model with a nonlocal boundary layer parameterization. *Rev. Geophys.,* **32,** 363–403, doi:10.1029/94RG01872.

Li, X., Y. Chao, J. McWilliams, and L.-L. Fu, 2001: A comparison of two vertical-mixing schemes in a Pacific Ocean general circulation model. *J. Climate,* **14,** 1377–1398, doi:10.1175/1520-0442(2001)014<1377:ACOTVM>2.0.CO;2.

Lien, R.-C., D. Caldwell, M. Gregg, and J. Moum, 1995: Turbulence variability at the equator in the central Pacific at the beginning of the 1991–1993 El Nino. *J. Geophys. Res.,* **100,** 6881–6898, doi:10.1029/94JC03312.

——, E. D'Asaro, and C. Menkes, 2008: Modulation of equatorial turbulence by tropical instability waves. *Geophys. Res. Lett.,* **35,** L24607, doi:10.1029/2008GL035860.

Lyman, J., D. Chelton, R. deSzoeke, and R. Samelson, 2005: Tropical instability waves as a resonance between equatorial Rossby waves. *J. Phys. Oceanogr.,* **35,** 232–254, doi:10.1175/JPO-2668.1.

——, G. Johnson, and W. Kessler, 2007: Distinct 17- and 33-day tropical instability waves in subsurface observations. *J. Phys. Oceanogr.,* **37,** 855–872, doi:10.1175/JPO3023.1.

Ma, C.-C., C. Mechoso, A. Arakawa, and J. Farrara, 1994: Sensitivity of a coupled ocean–atmosphere model to physical parameterizations. *J. Climate,* **7,** 1883–1896, doi:10.1175/1520-0442(1994)007<1883:SOACOM>2.0.CO;2.

MacDonald, D., and F. Chen, 2012: Enhancement of turbulence through lateral spreading in a stratified-shear flow: Development and assessment of a conceptual model. *J. Geophys. Res.,* **117,** C05025, doi:10.1029/2011JC007484.

Marchesiello, P., X. Capet, C. Menkes, and S. Kennan, 2011: Submesoscale dynamics in tropical instability waves. *Ocean Modell.,* **39,** 31–46, doi:10.1016/j.ocemod.2011.04.011.

Masina, S., S. Philander, and A. Bush, 1999: An analysis of tropical instability waves in a numerical model of the Pacific Ocean: 2. Generation and energetics of the waves. *J. Geophys. Res.,* **104,** 29 637–29 661, doi:10.1029/1999JC900226.

McPhaden, M., 2002: Mixed layer temperature balance on intraseasonal timescales in the equatorial Pacific Ocean. *J. Climate,* **15,** 2632–2647, doi:10.1175/1520-0442(2002)015<2632:MLTBOI>2.0.CO;2.

——, and Coauthors, 1998: The tropical ocean-global atmosphere observing system: A decade of progress. *J. Geophys. Res.,* **103,** 14 169–14 240, doi:10.1029/97JC02906.

Menkes, C., J. Vialard, S. Kennan, J. Boulanger, and G. Madec, 2006: A modeling study of the impact of tropical instability waves on the heat budget of the eastern equatorial Pacific. *J. Phys. Oceanogr.,* **36,** 847–865, doi:10.1175/JPO2904.1.

Moum, J., R.-C. Lien, A. Perlin, J. Nash, M. Gregg, and P. Wiles, 2009: Sea surface cooling at the equator by subsurface mixing in tropical instability waves. *Nat. Geosci.,* **2,** 761–765, doi:10.1038/ngeo657.

——, A. Perlin, J. Nash, and M. McPhaden, 2013: Seasonal sea surface cooling in the equatorial Pacific cold tongue controlled by ocean mixing. *Nature,* **500,** 64–67, doi:10.1038/nature12363.

Pacanowski, R., and S. Philander, 1981: Parameterization of vertical mixing in numerical models of tropical oceans. *J. Phys. Oceanogr.,* **11,** 1443–1451, doi:10.1175/1520-0485(1981)011<1443:POVMIN>2.0.CO;2.

Perez, R., M. Cronin, and W. Kessler, 2010: Tropical cells and a secondary circulation near the northern front of the equatorial Pacific cold tongue. *J. Phys. Oceanogr.,* **40,** 2091–2106, doi:10.1175/2010JPO4366.1.

Peters, H., M. Gregg, and J. Toole, 1988: On the parameterization of equatorial turbulence. *J. Geophys. Res.,* **93,** 1199–1218, doi:10.1029/JC093iC02p01199.

Philander, S., 1976: Instabilities of zonal equatorial currents. *J. Geophys. Res.,* **81,** 3725–3735, doi:10.1029/JC081i021p03725.

Price, J., R. Weller, and R. Pinkel, 1986: Diurnal cycling: Observations and models of the upper ocean response to diurnal heating, cooling, and wind mixing. *J. Geophys. Res.,* **91,** 8411–8427, doi:10.1029/JC091iC07p08411.

Qiao, L., and R. Weisberg, 1995: Tropical instability wave kinematics: Observations from the tropical instability wave experiment. *J. Geophys. Res.,* **100,** 8677–8693, doi:10.1029/95JC00305.

Seo, H., M. Jochum, R. Murtugudde, A. Miller, and J. Roads, 2007: Feedback of tropical instability-wave-induced atmospheric variability onto the ocean. *J. Climate,* **20,** 5842–5855, doi:10.1175/JCLI4330.1.

Shchepetkin, A., and J. McWilliams, 2005: The Regional Oceanic Modeling System (ROMS): A split-explicit, free-surface, topography-following-coordinate oceanic model. *Ocean Modell.,* **9,** 347–404, doi:10.1016/j.ocemod.2004.08.002.

Skyllingstad, E., and R. Samelson, 2012: Baroclinic frontal instabilities and turbulent mixing in the surface boundary layer. Part I: Unforced simulations. *J. Phys. Oceanogr.,* **42,** 1701–1716, doi:10.1175/JPO-D-10-05016.1.

Small, R., K. Richards, S.-P. Xie, P. Dutrieux, and T. Miyama, 2009: Damping of tropical instability waves caused by the action of surface currents on stress. *J. Geophys. Res.,* **114,** C04009, doi:10.1029/2008JC005147.

Smyth, W., and J. Moum, 2013: Marginal instability and deep cycle turbulence in the eastern equatorial Pacific Ocean. *Geophys. Res. Lett.,* **40,** 6181–6185, doi:10.1002/2013GL058403.

Thum, N., S. Esbensen, D. Chelton, and M. McPhaden, 2002: Air–sea heat exchange along the northern sea surface temperature front in the eastern tropical Pacific. *J. Climate,* **15,** 3361–3378, doi:10.1175/1520-0442(2002)015<3361:ASHEAT>2.0.CO;2.

Willett, C., R. Leben, and M. F. Lavín, 2006: Eddies and tropical instability waves in the eastern tropical Pacific: A review. *Prog. Oceanogr.,* **69,** 218–238, doi:10.1016/j.pocean.2006.03.010.

Zaron, E., and J. Moum, 2009: A new look at Richardson number mixing schemes for equatorial ocean modeling. *J. Phys. Oceanogr.,* **39,** 2652–2664, doi:10.1175/2009JPO4133.1.